Evidence of shallow band gap in ultrathin $1T'$-$MoTe_2$ via infrared spectroscopy

Jin Cheol Park,[1,2,*] Eilho Jung,[3,*] Sangyun Lee,[2] Jungseek Hwang,[3,†] and Young Hee Lee[1,2,3,‡]

[1]*Department of Energy Science, Sungkyunkwan University, Suwon 16419, Republic of Korea*

[2]*Center for Integrated Nanostructure Physics (CINAP), Institute for Basic Science (IBS), Suwon 16419, Republic of Korea*

[3]*Department of Physics, Sungkyunkwan University, Suwon 16419, Republic of Korea*

(Received 4 March 2020; revised manuscript received 1 June 2020; accepted 3 June 2020; published 22 June 2020)

Although van der Waals (vdW) layered MoS_2 shows the phase transformation from the semiconducting $2H$ phase to the metallic $1T$ phase through chemical lithium intercalation, vdW $MoTe_2$ is thermodynamically reversible between the $2H$- and $1T'$ phases, and can be further transformed by energetics, laser irradiation, strain or pressure, and electrical doping. Here, thickness- and temperature-dependent optical properties of $1T'$-$MoTe_2$ thin films grown by chemical vapor depsition are investigated via Fourier-transformed infrared spectroscopy. An optical gap of 28 ± 2 meV in a three-layer (or 2-nm)-thick $1T'$-$MoTe_2$ is clearly observed at a low-temperature region below 50 K. No discernible optical band gap is observed in samples thicker than ~4 nm. The observed thickness-dependent band-gap results agree with the measured dc resistivity data; the thickness-dependent $1T'$-$MoTe_2$ clearly demonstrates the metal-semiconductor transition at a crossover below the 2-nm-thick sample.

DOI: 10.1103/PhysRevB.101.235434

I. INTRODUCTION

Two-dimensional (2D) van der Waals (vdW) layered materials including graphene, hexagonal boron nitride (h-BN), and transition-metal dichalcogenides (TMDs) have demonstrated numerous intriguing physical phenomena including spin-orbit coupling, strong Coulomb interaction, large exciton binding energy, band-gap renormalization, direct to indirect band-gap transition, topological insulator, valleytronics, and metal-insulator transition [1–6]. Among 2D vdW layered materials, TMD materials have especially shown various phase-dependent crystal forms including $2H$-, $1T$-, $1T'$-, rhombohedral $3R$-, and orthorhombic T_d phases [7–9]. Various semiconducting $2H$ phases have received considerable attention because of their fascinating electrical and optical properties, e.g., indirect to direct band-gap crossover, large exciton binding energy, and spin-orbit splitting of excitons [10,11], together with the recently observed semimetallic states ($1T$-, $1T'$-, and T_d phases) for charge-density wave, unsaturated and giant magnetoresistance, and Weyl semimetal (WSM) [12,13].

$1T'$-Molybdenum ditelluride ($MoTe_2$) has been suggested as a type II WSM candidate [14–17], and recently proposed as a quantum spin-Hall (QSH) insulator [18]. The presence of band gap of ~0.1 eV, its value, and sensitivity to temperature are primary concern in the field of QSH-based devices for practical applications [19]. For practical applications, information of optical (or electronic) properties of thin-film $1T'$-$MoTe_2$ is important. Therefore, one needs to study thickness- and temperature-dependent optical properties of thin-film $1T'$-$MoTe_2$ to search for a band-gap opening.

Here, we report the thickness- and temperature-dependent optical properties of chemical vapor deposition (CVD)-grown $1T'$-$MoTe_2$ thin films via Fourier-transform infrared spectroscopy (FTIR). Temperature-dependent optical conductivity spectra of $1T'$-$MoTe_2$ films are observed for three different thicknesses of 2, 4, and 10 nm. We directly observe a narrow band gap of 28 ± 2 meV in a three-layer (or 2-nm)-thin $1T'$-$MoTe_2$ at temperature below 50 K; this narrow band gap is obscured by thermally excited charge carriers at temperatures above 80 K. Furthermore, these observations are congruent with the electrically measured dc resistivity data of the thin-film samples. Moreover, we discover the phase transition from the $1T'$- to T_d phase below 250 K for a thickness of above 10 nm.

II. SYNTHESIS AND CHARACTERISTICS OF $1T'$-$MoTe_2$ FILMS

A schematic of a two-zone CVD system was adopted to separately control the temperature and heating rate of both the Te-supplying (T_1) and -synthesis zones (T_2) [Fig. 1(a) and Fig. S1, Supplemental Material; details are provided in Methods) [20]. To characterize the CVD-grown $1T'$-$MoTe_2$ films, Raman spectroscopy is performed with a 532-nm wavelength laser. Two important vibration modes, A_g ($258-265\,cm^{-1}$) and B_g ($162-163\,cm^{-1}$) are observed in three different thickness samples. The position of B_g mode does not vary with thicknesses, while the position of A_g mode exhibits a blueshift from 258.8 to 265.0 cm^{-1} with decreasing thickness [Fig. 1(b)], which agrees with previous reports [21]. This implies that the samples are fully relaxed after transfer of the samples. To confirm the presence of strain, we measured Raman spectra (B_g mode) of $1T'$-$MoTe_2$ film samples before and after the transfer. No significant difference between two sets of B_g modes is observed (Fig. S2, Supplemental Material)

*These authors contributed equally to this work.
†jungseek@skku.edu
‡leeyoung@skku.edu

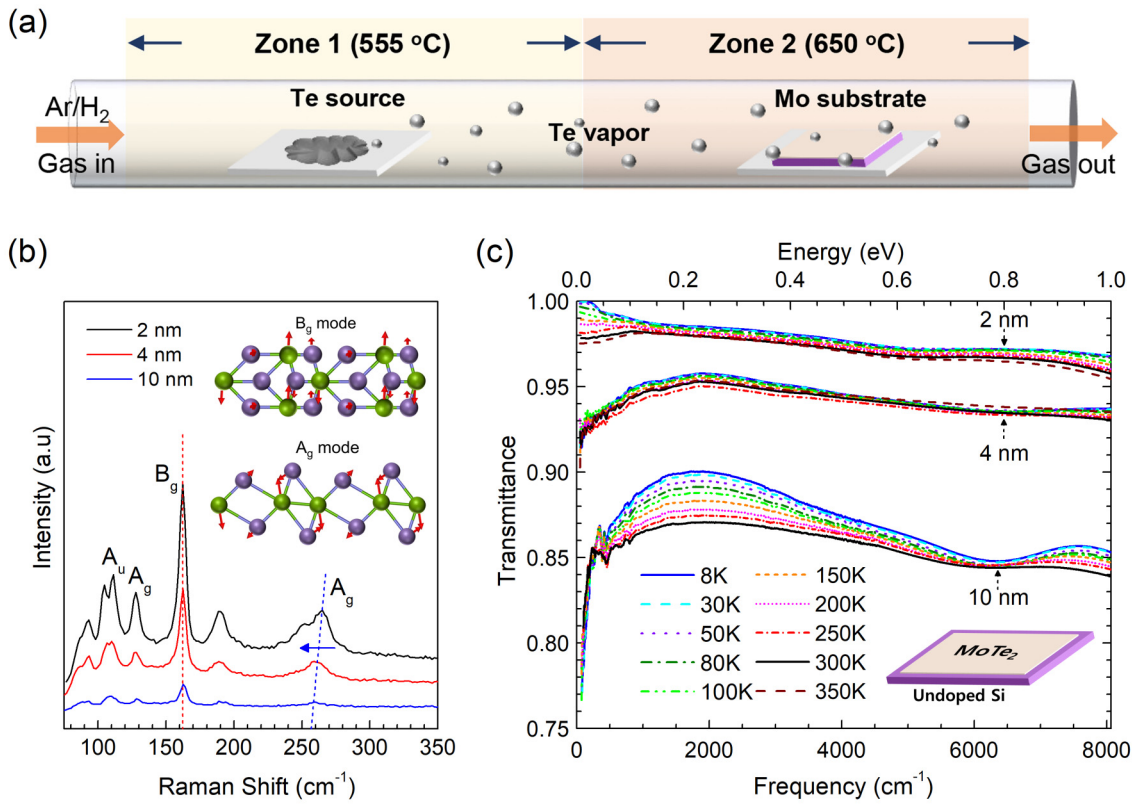

FIG. 1. Synthesis of $1T'$-$MoTe_2$ thin films and transmittance spectra. (a) A schematic of a two-zone chemical vapor deposition system to synthesize the $1T'$-$MoTe_2$ film on SiO_2/Si substrate. (b) Thickness-dependent Raman spectra for $1T'$-$MoTe_2$ with three different thicknesses (2, 4, and 10 nm). (c) Measured transmittance spectra for $1T'$-$MoTe_2$ films at various temperatures between 8 and 350 K.

[20]. Additionally, x-ray diffraction, transmission electron microscopy (TEM), and scanning transmission electron microscopy were used to characterize the thin-film samples in previous report [22].

III. OPTICAL MEASUREMENT AND DATA ANALYSIS

$1T'$-$MoTe_2$ films were prepared on a centimeter-scale double-side polished undoped Si substrate for optical study [Fig. 1(c)]. The transmittance spectra were measured with respect to the substrate [$T(\omega) = \frac{T_{\text{film/substrate}}}{T_{\text{substrate}}}$] where $T_{\text{film/substrate}}$ and $T_{\text{substrate}}$ are the transmittance spectra of the sample/substrate and substrate, respectively. We show the measured transmittance spectra [$T(\omega)$] of the three $1T'$-$MoTe_2$ samples with 2-, 4-, and 10-nm thicknesses at various temperatures [Fig. 1(c)]; transmittance increases in thinner $1T'$-$MoTe_2$ samples. The transmittance is reduced in the far-IR region below 400 cm^{-1} for thicknesses of 4 and 10 nm, showing a metallic behavior with a Drude component. In the same region, the transmittance increases at a thickness of 2 nm particularly in the low-temperature region below 200 K.

To further understand the distinct behaviors between a 2-nm-thin sample and thicker samples in the far-IR region, the optical conductivity is extracted from the observed transmittance spectra via the Tinkham formula, which can be written as $T(\omega) = \frac{1}{|1+\tilde{\sigma}(\omega)\, d\, \frac{Z_0}{n_s+1}|^2}$, where $T(\omega)$ is the transmittance with respect to the substrate, $\tilde{\sigma}(\omega) = \sigma_1(\omega) + i\sigma_2(\omega)$ is the complex optical conductivity, n_s is the index of refraction of the substrate, and Z_0 ($= 377\,\Omega$) is the impedance of the vacuum [23,24]. For very thin films on a thick substrate [$d \ll d_{\text{sub}}$, $d \ll \lambda$, and $d \ll \delta$, where d, d_{sub}, δ, and λ are the thicknesses of the film and the substrate, the skin depth (for metallic films), and the wavelength, respectively] the real part of the optical conductivity can be rewritten as $\sigma_1(\omega) \cong \frac{n_s+1}{Z_0 d}\left(\sqrt{\frac{1}{T(\omega)}} - 1\right)$. Here we note that the contribution of the imaginary part of the optical conductivity is negligible for metals in low-frequency region [24]. To further investigate the electronic structure, we used the Drude-Lorentz model; intraband and interband optical transitions can be described by their respective Drude and Lorentz components. The real part of the optical conductivity can be described in the Drude-Lorentz model as

$$\sigma_1(\omega) = \frac{1}{4\pi}\left[\frac{\omega_{pD}^2}{\tau(\omega^2+\tau^{-2})} + \sum_j \frac{\gamma_j \omega^2 \Omega_j^2}{\left(\omega_j^2-\omega^2\right)^2 + \gamma_j^2\omega^2}\right],$$

where ω_{pD} and τ^{-1} are the plasma frequency and impurity scattering rate of the Drude mode, respectively; Ω_j, ω_j, and γ_j are the plasma frequency, resonance frequency, and damping parameter of the jth Lorentz mode, respectively. Moreover, one can obtain the dc conductivity from the zero-frequency limit of the optical conductivity as $\sigma_1(0) = \frac{\omega_{pD}^2}{4\pi\tau^{-1}}$, which can be described by the Drude plasma frequency and scattering rate. The optical conductivity contains information of the electronic (band) structure; intraband transitions in the

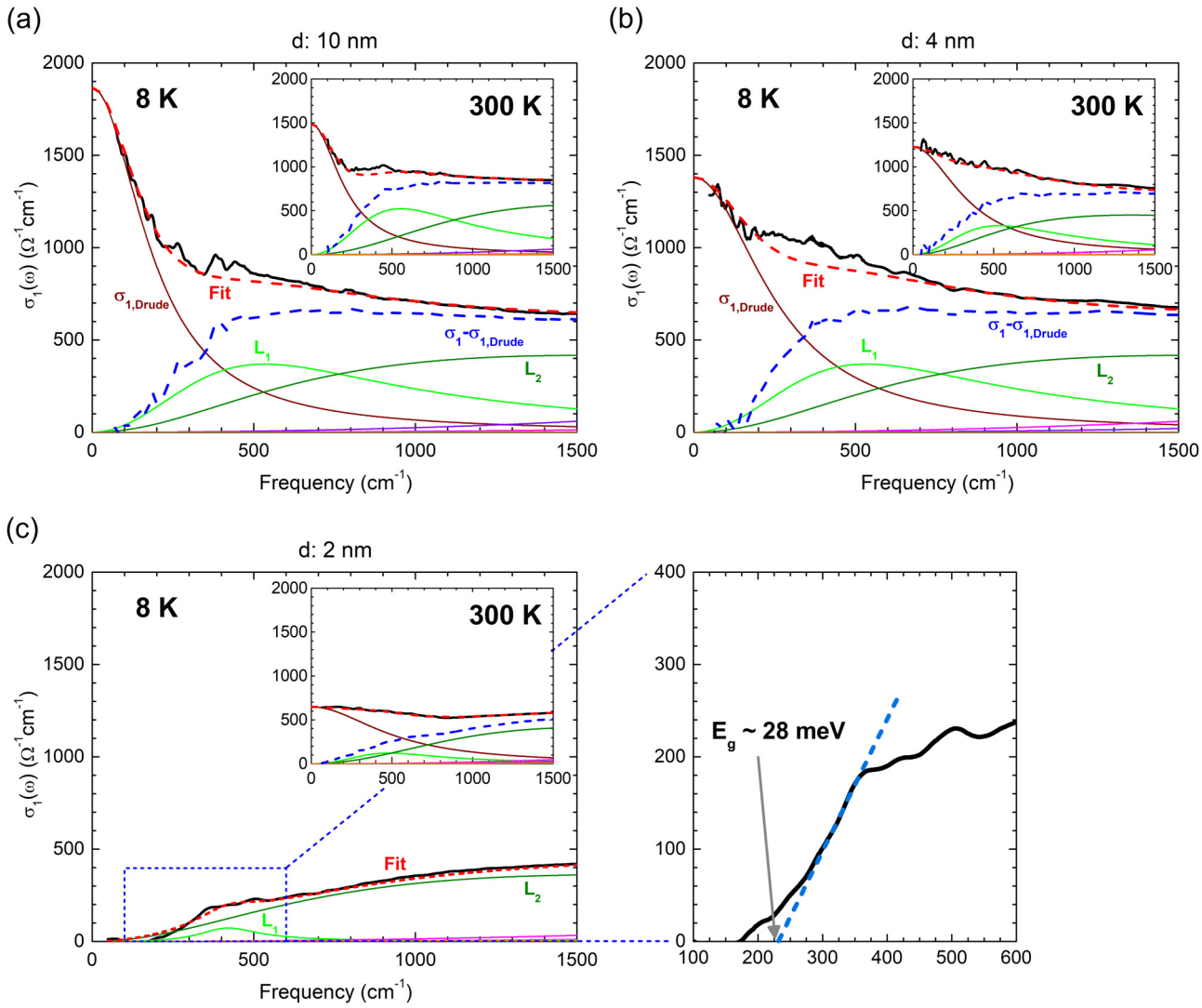

FIG. 2. Thickness- and temperature-dependent optical conductivity of $1T'$-$MoTe_2$ films. The real part of optical conductivity for (a) 10-nm-thick $1T'$-$MoTe_2$, (b) 4-nm-thick $1T'$-$MoTe_2$, and (c) 2-nm-thick $1T'$-$MoTe_2$ at 8 K. Each inset shows the corresponding real part of optical conductivity at 300 K.

partially filled bands are contributed from unbound electrons (or the Drude component), and interband transitions from the occupied bands to the unoccupied bands are contributed from bounded electrons (or the Lorentz components). The real part of the optical conductivity in the infrared region can be fitted using the Drude-Lorentz model.

IV. RESULTS AND DISCUSSION

The optical conductivities are extracted from the measured transmittance spectra of three different samples with thicknesses of 10, 4, and 2 nm at 8 and 300 K (inset) (Fig. 2, with more temperature points in Figs. S3–S6, Supplemental Material) [20]. Drude and Lorentz components are used for analyzing the optical conductivities in an entire range of frequencies up to 1500 cm^{-1}. The fitted results are shown with the dashed red lines, which are composed of one Drude component (the solid wine line) and a pair of Lorentz components (L_1 and L_2, the solid blue line denotes the optical conductivity without the Drude component) in Fig. 2. Drude components below 400 cm^{-1} are clearly observed in the optical conductivity at thicknesses of 10 and 4 nm [Figs. 2(a) and 2(b)]. In contrast, the Drude component is absent in the 2-nm-thick sample at 8 K [Fig. 2(c)]. From the optical conductivity in the 2-nm-thick sample, we extract an optical gap (E_g) of 28 ± 2 meV at 8 K. The error in the gap is roughly estimated from uncertainty of the linear extrapolation line (blue dashed line). The optical gap is closed at temperatures above 80 K.

Here we need to discuss about applicability of the Tinkham formula used for metallic samples, $\sigma_1(\omega) \cong \frac{n_s+1}{Z_0 d}\left(\sqrt{\frac{1}{T(\omega)}} - 1\right)$, to a spectrum with an energy gap because in this case the imaginary part of the conductivity [$\sigma_2(\omega)$] is not guaranteed to be negligibly small. However, it has been shown that for very thin semiconducting samples the imaginary part can be ignored [25]. Further detailed discussion on this issue is given in the Supplemental Material, Fig. S7 [20].

The fitting parameters of the Drude component are the plasma frequency, ω_{pD} and the impurity scattering rate, τ^{-1}

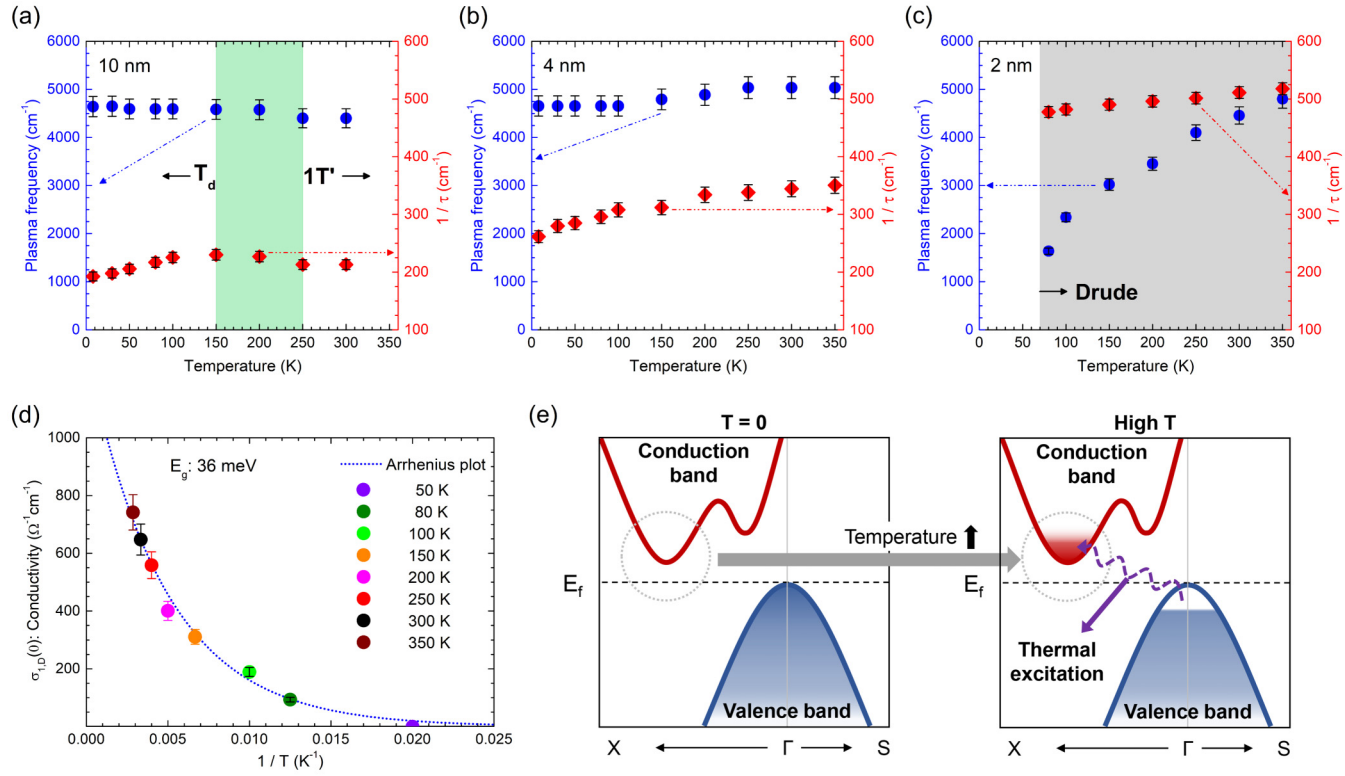

FIG. 3. Drude fitting parameters of $1T'$-$MoTe_2$ films. The plasma frequency (blue triangle) and scattering rate (red triangle) of the Drude component obtained from the Drude-Lorentz model fit as a function of temperature in (a) 10-nm-thick, (b) 4-nm-thick, and (c) 2-nm-thick $1T'$-$MoTe_2$. (d) The dc conductivity data obtained from a zero-frequency extrapolation of the optical conductivity and the fit (blue dotted line) as a function of $1/T$ at 2-nm-thick $1T'$-$MoTe_2$. (e) Schematics of electronic band structures near the Fermi level at $T = 0$ (left) and thermally promoted excitations at a finite temperature (right).

[Figs. 3(a)–3(c)]. For the 10-nm-thick $1T'$-$MoTe_2$ sample, the Drude plasma frequency (ω_{pD}) is slightly enhanced from 4400 to 4700 cm^{-1} below 250 K as the temperature decreases. Such an gradual rise of ω_{pD} at 250 K is associated with an emergence of a Weyl semimetallic state in the band structure, which takes place along with the structural phase transition from $1T'$- to T_d phase at approximately 200 K [8,26,27]. Similar behaviors are observed with charge-carrier densities varying from 1.49×10^{13} to 1.70×10^{13} cm^{-2} (Fig. S8, Supplemental Material) [20]. In contrast, the τ^{-1} decreases linearly from 230 cm^{-1} at 150 K to 192.5 cm^{-1} at 8 K, i.e., the Drude component becomes sharper, which is a characteristic of typical metals. For the 4-nm-thick $1T'$-$MoTe_2$, the plasma frequency (or charge-carrier density) and scattering rate monotonically decrease with decreasing temperature and become more prominent with monotonic frequency behavior in 2-nm-thick $MoTe_2$; this indicates that the T_d phase appears in bulk but vanishes in thin $MoTe_2$ film.

We describe the thermally induced dc conductivity in terms of the optical band gap (E_g) using the Arrhenius plot, $\sigma_{dc} = \sigma_0 \exp(-\frac{E_g}{2 \cdot k_B T})$, where σ_{dc} is the dc conductivity, σ_0 is the pre-exponential factor, k_B is the Boltzmann constant, and T is the absolute temperature [28,29]. The prefactor (1/2) in the exponent appears due to the possible distributions of electrons in the conduction band, independent of those of the valence-band holes. The dc conductivity for 2-nm-thick $1T'$-$MoTe_2$ sample yields $\sigma_0 = 1300 \pm 150\ \Omega^{-1}\ cm^{-1}$ and $E_g = 36 \pm 4$ meV [Fig. 3(d)]. The error in the gap is estimated by adjusting the fitting parameters for giving similar fitting quality. This is consistent with the optical gap obtained from the optical conductivity [see Fig. 2(c)]. Here we note that the optical gap (28 ± 2 meV) directly obtained from optical conductivity is more reliable compared with the one (36 ± 4 meV) obtained from the thermally induced dc conductivity.

We now demonstrate the experimental optical gap in our temperature-dependent spectroscopy. Our results are consistent with a finite band gap predicted by the theoretical band structure of monolayer $1T'$-$MoTe_2$ [Fig. 3(e)]. As the temperature increases, electrons in the valence band can be thermally excited to the conduction band, thus contributing to the conductivity. At temperatures above 80 K at 2-nm-thick $1T'$-$MoTe_2$, the optical conductivity includes a Drude component from these thermally excited electrons. One may concern static doping, which may be caused by possible impurities, in the samples prepared by CVD. We do not directly check whether our thin-film samples with thicknesses of 4 and 10 nm are statically doped or not. However, we can tell that the 2-nm-thick sample is not statically doped because we can clearly observe a small energy gap (28 ± 2 meV). Furthermore, since all samples were prepared by the same CVD method, we expect that all samples prepared by our CVD method are free from static doping.

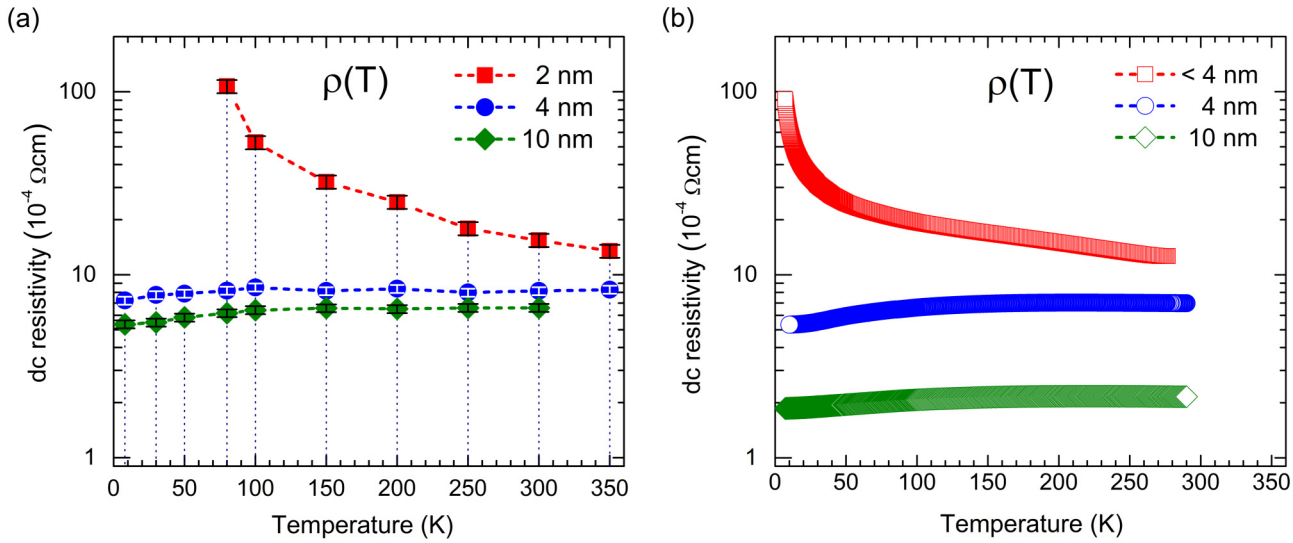

FIG. 4. Comparison of optical dc resistivity with directly measured dc transport resistivity. (a) Optically obtained dc resistivity data of $1T'$-$MoTe_2$ films with three different thicknesses as a function of temperature. (b) The directly measured dc resistivity data of the $1T'$-$MoTe_2$ films as a function of temperature.

Finally, we display the optically extracted dc resistivity data of our three $1T'$-$MoTe_2$ thin-film samples with their corresponding temperatures [Fig. 4(a)]. The dc resistivity data of 10- and 4-nm-thick $1T'$-$MoTe_2$ samples show metallic behaviors. Meanwhile, a semiconducting behavior emerges at 2-nm-thick $1T'$-$MoTe_2$ sample. This is a clear demonstration of a thickness-induced metal-semiconductor transition between 2 and 4 nm. We also measured the dc resistivity data using the van der Pauw method (details are described in Methods) [30]. Similar metal-semiconductor turnover is observed, although the absolute resistivity value varies from the optical gap approach [Fig. 4(b)]. The optically estimated resistivity may contain large uncertainty due to unavailable frequency below $\sim 70\,\mathrm{cm}^{-1}$ compared to directly measured dc resistivity; the conductivity fitted from Drude model may cause overestimation at zero-frequency limit.

We note that the small band gap of 28 ± 2 meV in 2-nm-thick $1T'$-$MoTe_2$ is different from previous reported 60 meV in exfoliated single-crystal $1T'$-$MoTe_2$ [21]. The previously measured band gap could be a mixed (or averaged) band gap of 1∼10-layered $1T'$-$MoTe_2$. It is of note that our samples grown by CVD might contain some amount of defects, which may smear the size of the band gap. To estimate the crystal quality, we provide the TEM images of top and side views of multilayer $1T'$-$MoTe_2$ film, indicating the presence of random Te vacancies (Fig. S9, Supplemental Material) [20].

V. CONCULSION

We have successfully studied the band-gap evolution of $1T'$-$MoTe_2$ with respect to both thickness and temperature. The Drude component becomes dominant at bulk samples (4- and 10-nm samples) in all temperature regions and at a thickness of 2 nm above 80 K. The T_d phase has appeared in the 10-nm-thick sample below 250 K. The 2-nm-thick $1T'$-$MoTe_2$ sample reveals an optical band gap of 28 ± 2 meV at 8 K that vanishes at temperatures above 80 K. The vanished band gap at high temperatures can be attributed to the thermally excited electrons from the valence to the conduction bands. Moreover, we have independently extracted a band gap of 36 ± 4 meV from the thermally induced dc conductivity. No band-gap opening is observed at 4- and 10-nm-thick samples at all selected temperatures between 8 and 350 K. Thickness-dependent $1T'$-$MoTe_2$ clearly demonstrates metal-semiconductor transition at a crossover below the 2 nm-thick sample. In addition, both the dc resistivity extracted from the optical conductivity spectra and that which was directly measured by the van der Pauw method show similar temperature-dependent behaviors [30]. Thus, our approach can be applied to other semimetallic two-dimensional layered materials for investigating their unique optical and electronic properties.

VI. METHODS

A. Synthesis of $1T'$-$MoTe_2$ films

To synthesize semimetallic $1T'$-$MoTe_2$ thin film, Mo thin films with thicknesses of 0.5, 1.3, and 4 nm were deposited on a 300-nm-thick SiO_2/Si substrate via a dc sputter. In a two-zone chemical vapor deposition system, a Te pellet of 0.5 g (Sigma-Aldrich) was placed in the first furnace zone and the Mo-deposited substrate was placed in the second furnace zone. To control the tellurization rate, the temperatures of the Te zone (T_1) and Mo film zone (T_2) were controlled separately. Before growing the $1T'$-$MoTe_2$ film, the whole CVD system was purged with 1000 sccm of argon (Ar) gas for 30 min to create an oxygen-free and Ar environment. During the growth process, Ar and hydrogen (H_2) gases were flown with rates of 100 and 20 sccm, respectively. T_1 and T_2 started heating up simultaneously with a ramping rate of T_1 reaching 555 °C first in 13 min and then T_2 reaching 650 °C in 15 min. When the T_2 temperature reached 650 °C, growth was carried out for 30 min under atmospheric pressure. After this growth, T_1 was cooled rapidly by opening the chamber; the T_2

chamber was opened 1 min after opening of the T_1 chamber to provide further cooling. During the cooling process, 500 sccm Ar and 20 sccm H_2 gases were introduced to remove the reactants. Finally, 2-, 4-, and 10-nm-thick $1T'$-$MoTe_2$ films were produced.

B. Transfer of $1T'$-$MoTe_2$ onto undoped Si substrate

To measure the FTIR spectra, the samples were transferred to undoped Si substrate using the conventional poly methyl methacrylate (PMMA) method [22,31]. To detach the grown $1T'$-$MoTe_2$ film from SiO_2/Si substrate on CVD, the PMMA-coated $1T'$-$MoTe_2$ film was floated on a buffered oxide etch (B.O.E., 1178-03, J.T. Baker) for 20 min. The PMMA/$1T'$-$MoTe_2$ film was then rinsed with distilled water several times after the SiO_2 part was completely etched by the B.O.E. solution. The resulting film was transferred onto an undoped Si substrate. After drying the film, the PMMA layer was eliminated by applying acetone and isopropyl alcohol.

C. Fourier-transform infrared spectroscopy

FTIR is an experimental technique to obtain the power spectrum in a wide infrared range from far- to near infrared. To measure the transmittance spectra of our samples we used a commercial FTIR spectrometer—Bruker Vertex 80v. The Vertex 80v is a vacuum-type spectrometer that is free from moisture and air absorptions. The spectrometer consists of three important components: a source, beam splitter, and detector. The configuration of the three components consists of a mercury arc lamp source, 6-micron multilayer Mylar beam splitter, and 4 K-bolometer detector for the far-infrared ($50-700\text{cm}^{-1}$ or 0.006–0.086 eV) range, a Globar lamp source, KBr beam splitter, and mercury-cadmium-telluride (MCT) or room temperature deuterated lanthanum triglycine sulphate (RT-DTGS) detector for mid-infrared ($400-7000\,\text{cm}^{-1}$ or 0.05–0.868 eV) range, and a tungsten lamp source, CaF_2 beam splitter, and InGaAs detector for near infrared ($4000-12\,000\,\text{cm}^{-1}$ or 0.5–1.5 eV). We used a commercial cold finger-type ARS optical cryostat and a commercial temperature controller (Lakeshore 325) to control the sample temperature both below and above room temperature. We used liquid helium as a coolant and were able to control the sample temperature from 8 to 350 K.

D. The dc transport resistivity measurement

The electrical resistivity was measured by the standard van der Pauw method. Platinum wires were attached by silver paste on each corner of the samples to provide a contact to the samples. The samples were cooled down by closed-cycle cryostat and measured using a Lake Shore Cryotronics® model 370 ac resistance bridge.

ACKNOWLEDGMENTS

This work was supported by the Institute for Basic Science of Korea (Grant No. IBS-R011-D1). J.H. acknowledges financial support from the National Research Foundation of Korea (Grant No. NRF-2017R1A2B4007387).

[1] A. K. Geim and K. S. Novoselov, Nat. Mater. **6**, 183 (2007).
[2] C. R. Dean, A. F. Young, I. Meric, C. Lee, L. Wang, S. Sorgenfrei, K. Watanabe, T. Taniguchi, P. Kim, K. L. Shepard, and J. Hone, Nat. Nanotechnol. **5**, 722 (2010).
[3] K. K. Kim, H. S. Lee, and Y. H. Lee, Chem. Soc. Rev. **47**, 6342 (2018).
[4] A. K. Geim and I. V. Grigorieva, Nature (London) **499**, 419 (2013).
[5] M. Chhowalla, H. S. Shin, G. Eda, L. J. Li, K. P. Loh, and H. Zhang, Nat. Chem. **5**, 263 (2013).
[6] K. S. Novoselov, A. Mishchenko, A. Carvalho, and A. H. C. Neto, Science **353**, aac9439 (2016).
[7] J. A. Wilson and A. D. Yoffe, Adv. Phys. **18**, 193 (1969).
[8] W. Dawson and D. Bullett, J. Phys. C: Solid State Phys. **20**, 6159 (1987).
[9] H. Yang, S. W. Kim, M. Chhowalla, and Y. H. Lee, Nat. Phys. **13**, 931 (2017).
[10] S. Z. Butler, S. M. Hollen, L. Y. Cao, Y. Cui, J. A. Gupta, H. R. Gutierrez, T. F. Heinz, S. S. Hong, J. X. Huang, A. F. Ismach, E. Johnston-Halperin, M. Kuno, V. V. Plashnitsa, R. D. Robinson, R. S. Ruoff, S. Salahuddin, J. Shan, L. Shi, M. G. Spencer, M. Terrones, W. Windl, and J. E. Goldberger, ACS Nano **7**, 2898 (2013).
[11] D. L. Duong, S. J. Yun, and Y. H. Lee, ACS Nano **11**, 11803 (2017).
[12] M. N. Ali, J. Xiong, S. Flynn, J. Tao, Q. D. Gibson, L. M. Schoop, T. Liang, N. Haldolaarachchige, M. Hirschberger, N. P. Ong, and R. J. Cava, Nature (London) **514**, 205 (2014).
[13] G. H. Han, D. L. Duong, D. H. Keum, S. J. Yun, and Y. H. Lee, Chem. Rev. **118**, 6297 (2018).
[14] A. Tamai, Q. S. Wu, I. Cucchi, F. Y. Bruno, S. Ricco, T. K. Kim, M. Hoesch, C. Barreteau, E. Giannini, C. Besnard, A. A. Soluyanov, and F. Baumberger, Phys. Rev. X **6**, 031021 (2016).
[15] J. Jiang, Z. K. Liu, Y. Sun, H. F. Yang, C. R. Rajamathi, Y. P. Qi, L. X. Yang, C. Chen, H. Peng, C. C. Hwang, S. Z. Sun, S. K. Mo, I. Vobornik, J. Fujii, S. S. P. Parkin, C. Felser, B. H. Yan, and Y. L. Chen, Nat. Commun. **8**, 13973 (2017).
[16] L. Huang, T. M. McCormick, M. Ochi, Z. Y. Zhao, M. T. Suzuki, R. Arita, Y. Wu, D. X. Mou, H. B. Cao, J. Q. Yan, N. Trivedi, and A. Kaminski, Nat. Mater. **15**, 1155 (2016).
[17] I. Belopolski, D. S. Sanchez, Y. Ishida, X. C. Pan, P. Yu, S. Y. Xu, G. Q. Chang, T. R. Chang, H. Zheng, N. Alidoust, G. Bian, M. Neupane, S. M. Huang, C. C. Lee, Y. Song, H. J. Bu, G. H. Wang, S. S. Li, G. Eda, H. T. Jeng, T. Kondo, H. Lin, Z. Liu, F. Q. Song, S. Shin, and M. Z. Hasan, Nat. Commun. **7**, 13643 (2016).
[18] X. F. Qian, J. W. Liu, L. Fu, and J. Li, Science **346**, 1344 (2014).
[19] S. S. Krishtopenko and F. Teppe, Sci. Adv. **4**, eaap7529 (2018).
[20] See Supplemental Material at http://link.aps.org/supplemental/10.1103/PhysRevB.101.235434 for details on optical and

atomic force microscopy (AFM) image, Raman spectra, optical conductivities, and Drude-Lorentz model fit at various temperature, analysis using transfer matrix method, charge-carrier density data, and TEM image.

[21] D. H. Keum, S. Cho, J. H. Kim, D.-H. Choe, H.-J. Sung, M. Kan, H. Kang, J.-Y. Hwang, S. W. Kim, H. Yang, K. J. Chang, and Y. H. Lee, Nat. Phys. **11**, 482 (2015).

[22] J. C. Park, S. J. Yun, H. Kim, J. H. Park, S. H. Chae, S. J. An, J. G. Kim, S. M. Kim, K. K. Kim, and Y. H. Lee, ACS Nano **9**, 6548 (2015).

[23] R. Glover III and M. Tinkham, Phys. Rev. **108**, 243 (1957).

[24] P. F. Henning, C. C. Homes, S. Maslov, G. L. Carr, D. N. Basov, B. Nikolić, and M. Strongin, Phys. Rev. Lett. **83**, 4880 (1999).

[25] J. Jo, E. Jung, J. C. Park, and J. Hwang, Curr. Appl. Phys. **20**, 237 (2020).

[26] A. N. Berger, E. Andrade, A. Kerelsky, D. Edelberg, J. Li, Z. J. Wang, L. Y. Zhang, J. Kim, N. Zaki, J. Avila, C. Y. Chen, M. C. Asensio, S. W. Cheong, B. A. Bernevig, and A. N. Pasupathy, npj Quantum Mater. **3**, 2 (2018).

[27] B. E. Brown, Acta Crystallogr. **20**, 268 (1966).

[28] S. Arrhenius, Z. Phys. Chem. **4U**, 96 (1889).

[29] S. Arrhenius, Z. Phys. Chem. **4U**, 226 (1889).

[30] L. J. van der Pauw, Philips Tech. Rev. **20**, 220 (1958).

[31] K. S. Kim, Y. Zhao, H. Jang, S. Y. Lee, J. M. Kim, K. S. Kim, J. H. Ahn, P. Kim, J. Y. Choi, and B. H. Hong, Nature (London) **457**, 706 (2009).